

ENHANCED MIXING IN GIANT IMPACT SIMULATIONS WITH A NEW LAGRANGIAN METHOD

HONGPING DENG,¹ CHRISTIAN REINHARDT,¹ FEDERICO BENITEZ,¹ LUCIO MAYER,¹ AND JOACHIM STADEL¹

¹*Center for Theoretical Astrophysics and Cosmology, Institute for Computational Science, University of Zurich, Winterthurerstrasse 190, 8057 Zurich, Switzerland*

(Received first draft; Revised; Accepted)

Submitted to ApJL

ABSTRACT

Giant impacts (GIs) are common in the late stage of planet formation. The Smoothed Particle Hydrodynamics (SPH) method is widely used for simulating the outcome of such violent collisions, one prominent example being the formation of the Moon. However, a decade of numerical studies in various areas of computational astrophysics have shown that the standard formulation of SPH suffers from several shortcomings, for example, its inability to capture subsonic turbulence, which can suppress mixing when two different fluids come into contact. In order to quantify how severe are these limitations when modeling GIs we did a comparison of simulations with identical initial conditions run with the standard SPH and a novel Lagrangian Meshless Finite Mass (MFM) method. We confirm the lack of mixing between the impactor and target when SPH is employed, while MFM is capable of driving turbulence and leads to significant mixing between the two bodies. Modern SPH variants with artificial conductivity, different formulation of the hydro force or reduced artificial viscosity, do not improve as significantly, and their initial conditions suffer from resolving density discontinuity at the core-mantle boundary.

Keywords: Giant impact, fluid mixing, numeric-Lagrangian method

1. INTRODUCTION

During the late stage of terrestrial planet formation, energetic collisions between roughly Mars-sized planetary embryos are common (Chambers 2001). These collisions are called giant impacts (GIs) and influence the mass, spin and number of planets in the final planetary system. The outcome of such violent collisions was studied in many previous publications (Asphaug et al. 2006; Leinhardt & Stewart 2012). One particularly interesting case is the giant impact hypothesis for the formation of the Moon (Cameron & Ward 1976; Benz et al. 1986; Canup & Asphaug 2001). The Moon and the Earth have almost identical isotope composition for several elements, such as oxygen (Wiechert et al. 2001) and titanium (Zhang et al. 2012). This is problematic as most previous simulations found that most disk silicates are derived from the impactor, which then must have had a composition almost identical to that of the Earth. Alternative models, a fast-spinning proto-Earth (Ćuk & Stewart 2012), a hit and run collision (Reufer et al. 2012) and an almost equal mass impact (Canup 2012) are proposed. However, all models are not fully satisfactory as they either fail to reproduce the observations or introduce new issues, for example, forming a fast spinning proto-Earth, that need to be solved.

Most GI simulations have used Smoothed Particle Hydrodynamics (SPH) (Lucy 1977; Gingold & Monaghan 1977). Many shortcomings of the method have been exposed and overcome in the last few years, such as artificial tension force at discontinuity (Agertz et al. 2007; Price 2008), excessive numerical viscosity (Cullen & Dehnen 2010), the noise associated with the kernel choice (Dehnen & Aly 2012), and the numerical dissipation of angular momentum (Kaufmann et al. 2007; Mayer et al. 2007; Deng et al. 2017). A new SPH scheme has been proposed (Hopkins 2013) and used in the moon formation GI simulation by Hosono et al. (2016). Special techniques for SPH are also developed in GI simulations, such as the treatment of free surface and the explicit conservation of entropy (Reinhardt & Stadel 2017). The numerical noise in SPH, including artificial viscosity, smears out physical motion and damps subsonic turbulence so improvements of the method are needed (Bauer & Springel 2012; Beck et al. 2016) which are absent in all previous giant impact simulations using SPH. (Hopkins 2015) implemented a new Lagrangian meshless finite mass (MFM) method in the GIZMO code showing very good shock capturing and conservation properties (Hopkins 2015; Deng et al. 2017). Hopkins (2015) also shows that MFM can capture small-scale turbulence and gives results very similar to moving-mesh and stationary-grid method (qualitatively and quantita-

tively). GIZMO MFM also appears to sustain subsonic MRI (Balbus & Hawley 1991) turbulence much longer than SPH in local shearing box simulations. (Deng et al. 2018, in prep)

We run GI simulations using the GIZMO code (Hopkins 2015), employing both MFM and SPH for different equations of state and planetary compositions, to investigate the role of the numerical hydrodynamics method on mixing in the post-impact remnant. The methods, initial conditions are described in section 2. We present the results of single component impacts in section 3.1 and multiple component impacts in section 3.2. We discuss the results in section 4 and draw conclusions in section 5.

2. INITIAL CONDITIONS AND HYDRODYNAMICAL METHODS

We use the GIZMO code (Hopkins 2015) which inherited SPH from the GADGET3 code (see Springel (2005) for GADGET2). We use the standard SPH with the Balsara switch, which is designed to minimize artificial viscosity away from shocks (Balsara 1995). We intentionally choose the standard SPH to enable comparison with previous work. We also present preliminary results with the improved Cullen & Dehnen artificial viscosity switch (Cullen & Dehnen 2010) and artificial thermal conductivity of Read & Hayfield (2012) in the discussion section. GIZMO also implements a new kind of Lagrangian MFM method which does effective volume partition according to the particle distribution and then solves the Riemann problem to update the fluid variables.

We build our initial conditions following Reinhardt & Stadel (2017) which gives a lower noise density representation of planet models when comparing to models generated from relaxation of a 3D lattice (Canup et al. 2013; Hosono et al. 2016). If needed, the resulting bodies are relaxed with the corresponding hydro-method (SPH/MFM) for about 3 hours until the root mean square velocity is less than 1% of the impact velocity as done in previous work. In order to avoid problems at the planet's surface while relaxing the model, we applied the free surface treatment proposed in (Reinhardt & Stadel 2017) but disabled it during the impact simulation to allow a direct comparison to prior results.

We use the Tillotson equation of state (EOS) (Tillotson 1962) for an impact of undifferentiated objects and MANEOS (Melosh 2007) for the canonical moon formation impact model (differentiated, 30% iron and 70% dunite by mass). We show that insufficient mixing in the SPH simulations is due to the hydro-method instead of the EOS or core-mantle boundary treatment.

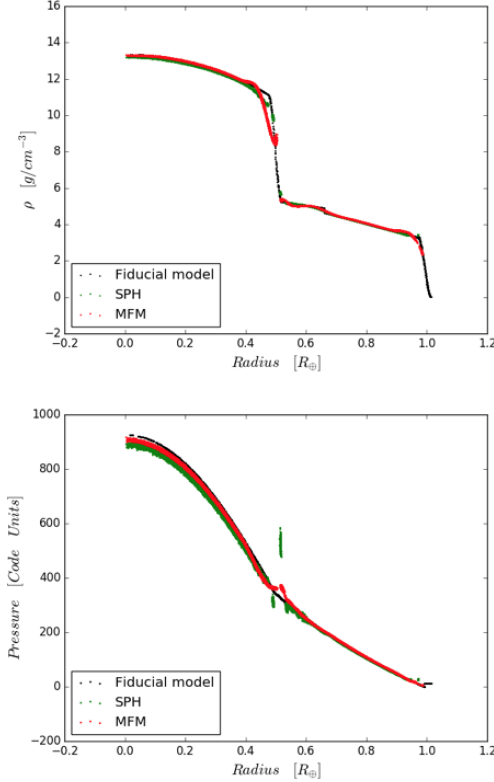


Figure 1. The density (upper panel) and pressure (lower panel) profile of the $0.89M_{\oplus}$ target in the *benchmark* moon formation run199 of Barr (2016). The initial condition is modeled with 500K particles of equal mass. The CTH grid code model (fiducial model), SPH model and MFM model are shown in black, green and red respectively. Some particles/cells enter an unphysical state in the core-mantle transition region in all three models with the SPH model showing a non-continuous pressure profile at the core-mantle boundary.

We describe our core-mantle boundary treatment in the following section.

2.0.1. Core-mantle boundary

We use 500K particles (comparable to recent high-resolution impact simulations) to sample the proto-Earth ($0.89M_{\oplus}$) in the canonical moon formation scenario and compare our model with the benchmark model of the moon formation impact, using the grid based hydro-code CTH (Crawford et al. 2006), proposed by Barr (2016) (private communication). In SPH,

$$\rho_i = \sum_j m_j W(|\mathbf{r}_i - \mathbf{r}_j|, h_i), \quad (1)$$

the density of the i th particle is the kernel weighted sum of its neighbour particles' masses, (Springel 2005) so the core-mantle boundary is not infinitely sharp. The core-mantle transition is at the smoothing length scale in SPH while MFM has a larger transition region (see the

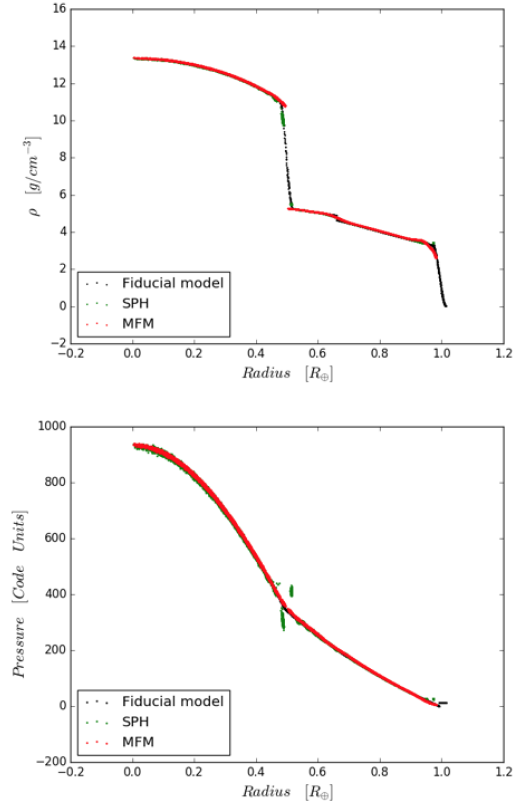


Figure 2. The density (upper panel) and pressure (lower panel) profile of the $0.89M_{\oplus}$ target in the *benchmark* moon formation run199 of Barr (2016). The initial condition is modeled using 500K particles with iron particles equal two times dunite particles' mass. The CTH grid code model (fiducial model), SPH model and MFM model are shown in black, green and red respectively. Only the MFM model keeps the infinitely sharp (no low-density iron particles) core-mantle transition while the SPH model still has non-continuous pressure profile at the core-mantle boundary.

upper panel of figure 1). Particles/cells in the transition region with density intermediate between iron density and dunite density, do not have well defined physical properties. They are *expanded iron* or *compressed dunite* in the EOS table which is not physical in the proto-Earth model.

Even worse, at the core-mantle boundary the density, thus the smoothing length, changes sharply, which leads to an artificial tension force separating the two components in standard SPH.(Agertz et al. 2007; Price 2008). In the lower panel of figure 1, we observe a non-continuous pressure (returned by the MANEOS EOS) profile in the SPH model due to the artificial tension force while MFM has a continuous pressure profile (although there remains a small pressure bump). This tension force harms fluid mixing but helps to keep a sharper

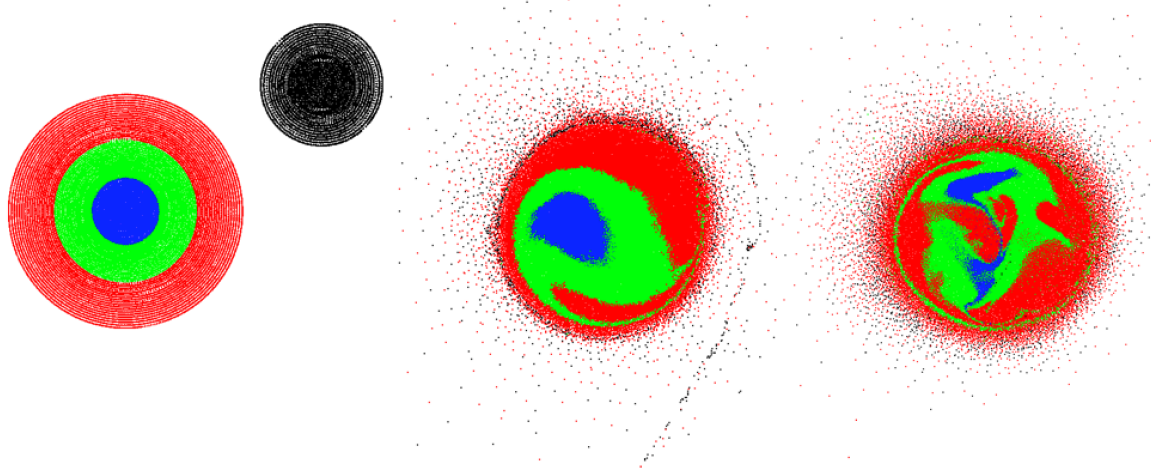


Figure 3. The left panel shows color-labeled different layers (slice between $-0.1 < z < 0.1$) of the pre-impact target and the impactor. The inner structure of the post-impact target (slice between $-0.1 < z < 0.1$) at $t = 13.8\text{ h}$ are shown in the middle (run with SPH) and right (run with MFM) panel. The inner core is disrupted and even some particles from the impactor get into the core region in the MFM simulation while the SPH simulation only show moderate deformation of the target.

core-mantle boundary in standard SPH than in MFM, see figure 1.

Woolfson (2007) proposed an extra correction factor for density at the interface between different components to maintain a sharp core-mantle transition. There is no clear indication that such a correction is self-consistent in the SPH or MFM formulation. Instead we use different mass particles in our MFM model. In MFM,

$$\rho_i = \frac{m_i}{V_{\text{eff},i}}, \quad (2)$$

where $V_{\text{eff},i}$ is the effective volume of the i th particle, see Hopkins (2015) for details. Using iron particles of mass two times that of the dunite particles', the smoothing length, thus V_{eff} , is almost continuous across the core-mantle boundary but we obtain sharp core-mantle boundary with no particles entering an unphysical state (see figure 2 upper panel). Woolfson (2007) varies the correction factor according to the density ratio of the two components but we simply use a 2:1 mass ratio of particles because moderate variation in the density ratio is tolerable but varying particle mass breaks the method. In figure 2, the pressure is still continuous in the MFM model and overlaps with the fiducial model, while the SPH model still suffers artificial tension force and has particles entering unphysical states. In the impact simulations, we use different mass particles in MFM but the same mass particles for SPH to enable direct comparison with prior work. Alternative SPH formulation (Ott & Schnetter 2003) based on discretizing the particle density instead of mass density, which is similar to MFM in density calculation, can also resolve the sharp

core-mantle boundary but has gained little attention in the giant impact community.

We note that we use different mass particles for iron and dunite but that these masses are exactly the same in both the impactor and target. Using different iron/dunite particle masses in the impactor and target can lead to numerical differentiation and thus cause unphysical mixing in our test runs with MFM.

3. RESULTS

3.1. Single component impact

For the single component models, we use the Tillotson EOS because it is simple and highly reliable. It can accurately model shocks, which are very important in hypervelocity impacts, and shows good agreement to measured data (Brundage 2013). Its main weakness is the lack of a thermodynamically consistent treatment of vaporization, which is not an issue in this simulation as we mainly focus on the different inner structure of the post-impact target here.

We use 500K particles to represent a M_{\oplus} target and a $0.1M_{\oplus}$ impactor, both of which are composed of granite described by the Tillotson EOS. This one component model is free of core-mantle discontinuity which is hard to handle in numeric models, see the discussion in section 2.0.1. The impact setup is similar to the canonical moon formation impact. The impact velocity equals 10 km/s and the impact parameter $b = 0.71$. We run this simple impact with both SPH and MFM in the GIZMO code where the only difference is the hydro-method.

We observe a striking difference in the inner structure of the post-impact target. In figure 3, we mark

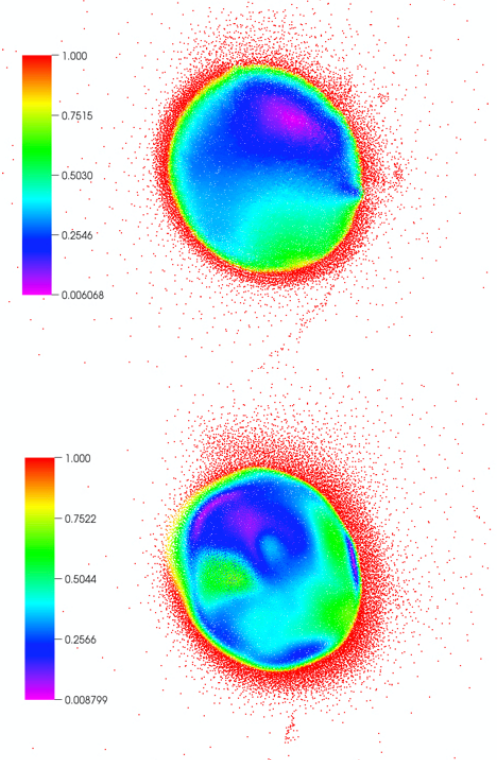


Figure 4. The velocity magnitude (km/s) of the $-0.1 < z < 0.1$ region in the major body. The snapshots are taken at $t = 10.5 h$ and some clumps are still re-colliding with the major body. The upper panel is the SPH simulation and the lower panel is MFM simulation. MFM is able to capture the more complex subsonic turbulence while SPH tends to damp it, resulting in a flow rotating around a low-velocity center.

three layers of the pre-impact target and the impactor with four different colors to trace the deformation of the target and the spread of the impactor. In the SPH simulation, the target’s core deforms slightly while in the MFM simulation the core is dispersed throughout the body. In the SPH simulation the outermost layer is strongly deformed but never gets into the core region. MFM is able to mix materials from the outmost layer of the target and some of the impactor into the core region.

This mixing happens as a result of complex 3D subsonic turbulence with typical velocity less than $1km/s$. We show the velocity field around the $z = 0$ plane after the giant impact in figure 4. In the SPH run the flow is almost laminar and simply circulates around a low-velocity center. The flow structure is influenced by the tidal force from the ejecta and the re-collision of the ejecta, but we always observe significantly more substructure in the flow characterizing the post-impact target in the MFM run. Bauer & Springel (2012) shows that standard SPH suppresses subsonic turbulence as does the pressure-entropy SPH implementation of Hopkins (2015). MFM, with no artificial viscosity, captures subsonic turbulence and agrees well with grid based code (Hopkins 2015). In the following section we assess the importance of capturing subsonic turbulence mixing in the canonical moon formation impact.

3.2. Multiple components impact

We run the run119 described by Canup et al. (2013) with SPH and MFM using 500K particles. In this impact, a $0.89M_{\oplus}$ target is hit by a $0.13M_{\oplus}$ impactor at their mutual escape velocity $\sim 9km/s$. This model was proposed as a benchmark by Barr (2016). Our initial condition is almost identical to that in such previous work.

3.2.1. Protolunar disk property

We do the disk analysis following Canup et al. (2013). We calculate the disk mass M_D and disk angular momentum L_D at $t = 35 h$, when the properties of the disk no longer change significantly. In our SPH simulation, we get disk mass $M_D = 1.70M_L$ and angular momentum of the disk $L_D = 0.35L_{EM}$ comparing well to $M_D = 1.69M_L$ and $L_D = 0.33L_{EM}$ in the highest resolution run199 of Canup et al. (2013). Here M_L and L_{EM} are, respectively, the moon mass and the angular momentum of the Earth-Moon system. Our SPH simulation agrees very well with previous SPH simulations. In our MFM simulation, we have $M_D = 1.86M_L, L_D = 0.37L_{EM}$. Both the disk mass and the angular momentum are higher than in the SPH simulation, which we attribute to better angular momentum conservation in MFM in differentially rotating flows (Deng et al. 2017). In the disk, the iron fraction is 7% in our SPH simulation, exactly as that in run199 of Canup et al. (2013), and the MFM simulation has an iron fraction of 4%.

3.2.2. Mixing

In the canonical moon formation scenario, part of the impactor material avoids directly colliding with the target due to its position offset and is sheared into spiral ejecta. The ejecta will contract and re-collide with the target and lead to the tidal disruption of the former and the formation of the disk. In this model most of the disk matter comes from the tidal disruption of the impactor. In run119 of Canup et al. (2013), 70% of the disk material originates from the impactor.

Following Reufer et al. (2012) we use the deviation factor δ_T to characterize the mixing in the moon for-

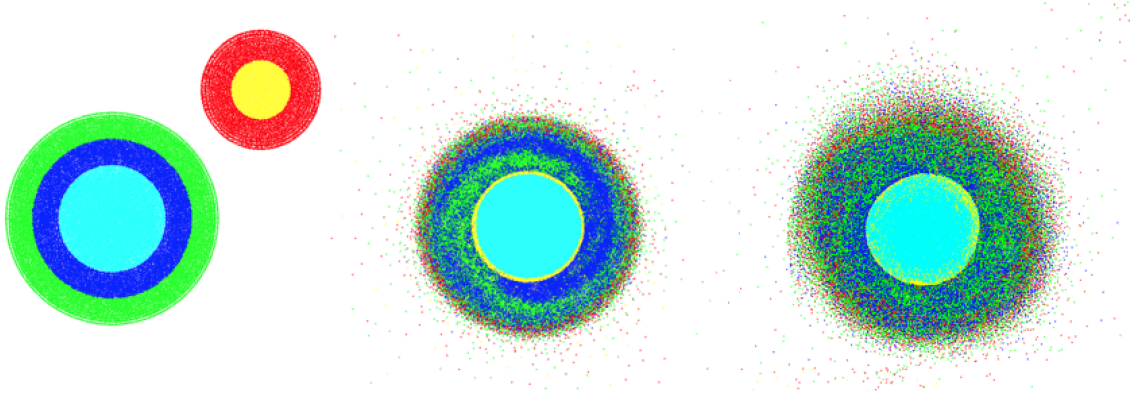


Figure 5. Left panel, color-labeled different layers (slice between $-0.1 < z < 0.1$) of the pre-impact target and the impactor. The material distribution between $-0.1 < z < 0.1$ of the single component impact at $t = 36\text{ h}$ are in the middle (run with SPH) and $t = 14\text{ h}$ right (run with MFM). In the SPH simulation, particles from the impactor mantle stay on the surface of the post-impact target due to the artificial tension force at the surface of the target and suppression of turbulence in the inner part of the target, which is also shown in (Emsenhuber et al. 2017). However, MFM mixes the post-impact target thoroughly and quickly. MFM has a puffy planet surface as is also observed for the density independent SPH implementation of Hosono et al. (2016).

mation giant impact, where

$$f_T = (M_{\text{targ}}^{\text{silc}}/M_{\text{tot}}^{\text{silc}})_{\text{disk}}, \quad (3)$$

$$\delta f_T = \frac{(M_{\text{targ}}^{\text{silc}}/M_{\text{tot}}^{\text{silc}})_{\text{disk}}}{(M_{\text{targ}}^{\text{silc}}/M_{\text{tot}}^{\text{silc}})_{\text{post-impactTarget}}} - 1. \quad (4)$$

$M_{\text{targ}}^{\text{silc}}$ and $M_{\text{tot}}^{\text{silc}}$ denote the mass of the silicate part of the disk/post-impact target derived from the target and the total disk/post-impact target mass, respectively. δf_T measures the compositional similarity between the silicate part of the proto-lunar disk and the post-impact target. In our SPH simulation, $f_T = 27\%$, $\delta f_T = -70\%$ agrees well with $f_T \approx 30\%$ in Reufer et al. (2012); Canup et al. (2013). In the MFM simulation $f_T = 43\%$, $\delta f_T = -50\%$ and there is a higher degree of mixing.

We can see the different mixing in the two methods in figure 5 clearly. We color label two layers of the proto-Earth mantle, core and impactor's mantle and core to trace the components. In the SPH simulation, the two layers of the mantle are distorted and become intertwined but do not mix (see snapshot taken at $t = 36\text{h}$). However, MFM mixes the two layers of the proto-Earth mantle and the impactor mantle thoroughly and quickly (snapshot taken at $t = 14\text{h}$). We tested that the SPH results are weakly dependent on the adoption of identical or different particle masses across the interface since we used MFM with two different particle masses. In both cases, SPH gives similar results and mixing is much less efficient than in MFM. SPH with 2:1 iron/rock mass particles gives $f_T = 30\%$ and $\delta f_T = -67\%$

The mixing in the moon formation simulation is much more pronounced than in the single component model in figure 3. The iron core can reflect pressure waves

and shorten the crossing time scale in the post-impact target and make mixing in the post-impact target easier. The tidal interaction between the core and mantle also drives turbulence and enhances mixing. In the SPH simulations, silicates from the impactor always stay on the surface of the post-impact target. They come from re-collided ejecta. Artificial tension force (see 2.0.1) prevent them entering the inner part of the post-impact target (Hosono et al. 2016) and the suppression of turbulence in the post-impact target (see 3.1) prevent them from mixing with the target. Some re-collided clumps are able to accelerate materials in the surface layer of the target onto disk orbits so in SPH simulation more materials from the impactor are put onto orbit in this process. MFM mixes the impactor's mantle and the target quickly and thus more silicates from the target can be propelled to the proto-lunar disk.

4. DISCUSSION: VARIANTS OF THE SPH METHOD

In the previous sections we have shown how MFM can resolve subsonic turbulence and the associated mixing in GIs, which instead standard SPH cannot achieve. The artificial tension force of standard SPH prevents fluid mixing, which in turn prevents re-collided ejecta mixing with the post-impact target (section 3.2.2). It can be alleviated by introducing artificial conductivity (Price 2008; Read & Hayfield 2012) or more accurate integral-based gradient estimator (Garca-Senz, D. et al. 2012; Rosswog 2015). We run the run119 with the artificial conductivity of Read & Hayfield (2012) and the mixing in the post-impact target is marginally improved with the impactor's mantle penetrating a little deeper and the

long distorted two layers of the target's mantle break into pieces. This artificial conductivity results in iron particles floating on the post-impact target's surface and the reason for this remains unclear. It may be related to the complicated EOS and thermal state. No notable difference is caused by the different artificial viscosity switches as well.

Hopkins (2015) also shows the pressure-entropy formulation of SPH does not help to sustain subsonic turbulence, although Wadsley et al. (2017) shows considerable benefits when that is combined with higher order kernels and a diffusion term. However, Beck et al. (2016) shows their improved Cullen & Dehnen switch helps to sustain subsonic turbulence. All these SPH variants incorporate modifications in many aspects of the implementation, none of which alone is capable of solving the issues highlighted in this paper, while MFM appears to capture turbulence and mixing by design, which makes it a highly competitive technique to simulate GIs.

5. CONCLUSIONS AND PERSPECTIVES

We used both SPH and, for the first time, a new Lagrangian method (MFM) to carry out GI simulations. In our single component model with the TILLOTSON EOS, we find SPH suppresses turbulence and thus mixing in the simulation. We run the canonical moon formation model with the MANEOS EOS. Our MFM initial conditions accurately model the core-mantle boundary with no particles entering an unphysical state. Our SPH

results are almost identical to those in the literature and our MFM simulations also agrees well in the disk mass and angular momentum with SPH simulations. Our MFM simulations show a large increase in the mixing between the impactor and the target. MFM is a well established hydrodynamics method with no immediately obvious flaws that would exaggerate the mixing seen in these simulations, rather, the indication from this work is that prior simulation results have underpredicted the amount of mixing taking place within real GIs. However, the moon formation model considered here has still a disk mostly originating from the impactor, an outcome which reflects the geometry of the encounter. Fully resolving the isotope conundrum arising in the the moon formation giant impact theory (Asphaug 2014) likely requires different initial conditions for the encounter. Hit-and-run models, for example, those in Reufer et al. (2012), could potentially result in a more efficient mixing. Overall MFM would seem the ideal method to pursue, in the near future, studies of mixing under a variety of initial conditions of GIs. Therefore MFM is not only a very competitive technique but holds promise to revolutionize our understanding of GIs. This work simply represents the first step in this direction.

We thank Amy Barr, Stephan Rosswog, Philip Hopkins, Martin Jutzi for useful discussion. We acknowledge support from the Swiss National Science Foundation via the NCCR PlanetS.

Software: GIZMO code (Hopkins 2015)

REFERENCES

Agertz, O., Moore, B., Stadel, J., et al. 2007, *Mon. Not. R. Astron. Soc.*, 380, 963

Asphaug, E. 2014, *Annual Review of Earth and Planetary Sciences*, 42, 551

Asphaug, E., Agnor, C. B., & Williams, Q. 2006, *Nature*, 439, 155

Balbus, S. A., & Hawley, J. F. 1991, *ApJ*, 376, 214

Balsara, D. S. 1995, *Journal of Computational Physics*, 121, 357

Barr, A. C. 2016, *Journal of Geophysical Research: Planets*, 121, 1573

Bauer, A., & Springel, V. 2012, *Monthly Notices of the Royal Astronomical Society*, 423, 2558

Beck, A. M., Murante, G., Arth, A., et al. 2016, *Mon. Not. R. Astron. Soc.*, 455, 2110

Benz, W., Slattery, W., & Cameron, A. 1986, *Icarus*, 66, 515

Brundage, A. L. 2013, *Procedia Engineering*, 58, 461

Cameron, A. G., & Ward, W. R. 1976, in *Lunar and Planetary Science Conference*, Vol. 7

Canup, R. M. 2012, *Science*, 338, 1052

Canup, R. M., & Asphaug, E. 2001, *Nature*, 412, 708

Canup, R. M., Barr, A. C., & Crawford, D. A. 2013, *Icarus*, 222, 200

Chambers, J. 2001, *Icarus*, 152, 205

Crawford, D., Taylor, P., Bell, R., & Hertel, E. 2006, , 25, 72

Ćuk, M., & Stewart, S. T. 2012, *Science*, 338, 1047

Cullen, L., & Dehnen, W. 2010, *Mon. Not. R. Astron. Soc.*, 408, 669

Dehnen, W., & Aly, H. 2012, *Mon. Not. R. Astron. Soc.*, 425, 1068

Deng, H., Mayer, L., & Meru, F. 2017, *The Astrophysical Journal*, 847, 43.

<http://stacks.iop.org/0004-637X/847/i=1/a=43>

Emsenhuber, A., Jutzi, M., & Benz, W. 2017, *Icarus*

Garca-Senz, D., Cabezn, R. M., & Escartn, J. A. 2012, *A&A*, 538, A9

Gingold, R. A., & Monaghan, J. J. 1977, *Monthly Notices of the Royal Astronomical Society*, 181, 375

Hopkins, P. F. 2013, *Mon. Not. R. Astron. Soc.*, 428, 2840

—. 2015, *Monthly Notices of the Royal Astronomical Society*, 450, 53

Hosono, N., Saitoh, T. R., Makino, J., Genda, H., & Ida, S. 2016, *Icarus*, 271, 131

Kaufmann, T., Mayer, L., Wadsley, J., Stadel, J., & Moore, B. 2007, *MNRAS*, 375, 53

Leinhardt, Z. M., & Stewart, S. T. 2012, *The Astrophysical Journal*, 745, 79

Lucy, L. B. 1977, *The astronomical journal*, 82, 1013

Mayer, L., Kazantzidis, S., Madau, P., et al. 2007, *Science*, 316, 1874

Melosh, H. 2007, *Meteoritics & Planetary Science*, 42, 2079

Ott, F., & Schnetter, E. 2003, *ArXiv Physics e-prints*, physics/0303112

Price, D. J. 2008, *Journal of Computational Physics*, 227, 10040

Read, J., & Hayfield, T. 2012, *Monthly Notices of the Royal Astronomical Society*, 422, 3037

Reinhardt, C., & Stadel, J. 2017, *Monthly Notices of the Royal Astronomical Society*, 467, 4252

Reufer, A., Meier, M. M., Benz, W., & Wieler, R. 2012, *Icarus*, 221, 296

Rosswog, S. 2015, *Monthly Notices of the Royal Astronomical Society*, 448, 3628

Springel, V. 2005, *Monthly notices of the royal astronomical society*, 364, 1105

Tillotson, J. H. 1962, *Metallic equations of state for hypervelocity impact*, Tech. rep., GENERAL DYNAMICS SAN DIEGO CA GENERAL ATOMIC DIV

Wadsley, J. W., Keller, B. W., & Quinn, T. R. 2017, *ArXiv e-prints*, arXiv:1707.03824

Wiechert, U., Halliday, A., Lee, D.-C., et al. 2001, *Science*, 294, 345

Woolfson, M. 2007, *Monthly Notices of the Royal Astronomical Society*, 376, 1173

Zhang, J., Dauphas, N., Davis, A. M., Leya, I., & Fedkin, A. 2012, *Nature Geoscience*, 5, 251